

Morphological evolution of $z \sim 1$ galaxies from deep K-band AO imaging in the COSMOS deep field $\star, \star\star$

M. Huertas-Company^{1,4}, D. Rouan¹, G. Soucail², O. Le Fèvre³, L. Tasca³, T. Contini²

¹ LESIA-Paris Observatory, 5 Place Jules Janssen, 92195 Meudon - France
e-mail: marc.huertas@obspm.fr

² Laboratoire d'Astrophysique de Toulouse-Tarbes, CNRS-UMR 5572 and Université Paul Sabatier Toulouse III, 14 Avenue Belin, 31400 Toulouse, France

³ LAM-Marseille Observatory, Traverse du Siphon-Les trois Lucs BP8-13376 Marseille Cedex 12 -France

⁴ IAA-C/ Camino Bajo de Huétor, 50 - 18008 Granada-Spain

Received ;date; / Accepted ;date;

ABSTRACT

Context. We present the results of an imaging programme of distant galaxies ($z \sim 0.8$) at high spatial resolution ($\sim 0.1''$) aiming at studying their morphological evolution. We observed 7 fields of $1' \times 1'$ with the NACO Adaptive Optics system (VLT) in Ks ($2.16\mu\text{m}$) band with typical $V \sim 14$ guide stars and 3h integration time per field. Observed fields are selected within the COSMOS survey area, in which multi-wavelength photometric and spectroscopic observations are on-going

Aims. High angular resolution K-band data have the advantage to probe old stellar populations in the rest-frame, enabling to determine galaxy morphological types unaffected by recent star formation, better linked to the underlying mass than classical optical morphology studies (HST). Adaptive optics on ground based telescopes is the only method today to obtain such high resolution in the K-band but it suffers from limitations since only small fields are observable and long integration times are necessary. In this paper we show that reliable results can however be obtained and establish a first basis for larger observing programmes.

Methods. We analyze the morphologies by means of B/D (Bulge/Disk) decomposition with GIM2D and CAS (Concentration-Asymmetry) estimators for 79 galaxies with magnitudes between $K_s = 17 - 23$ and classify them in three main morphological types (Late Type, Early Type and Irregulars). Automated and objective classification allows a precise error estimation. Simulations and comparisons with seeing limited (CFHT/Megacam) and space (HST/ACS) data have been carried out to evaluate the accuracy of adaptive optics based observations for morphological purposes.

Results. We obtain for the first time an estimate of the distribution of galaxy types at redshift $z \sim 1$ as measured from the near infrared at high spatial resolution. We show that galactic parameters (disk scale length, bulge effective radius and bulge fraction) can be estimated with a random error lower than 20% for the bulge fraction up to $K_s = 19$ ($AB = 21$) and that classification into the three main morphological types can be done up to $K_s = 20$ ($AB = 22$) with at least 70% of correct identifications. We used the known photometric redshifts to obtain a redshift distribution over 2 redshift bins ($z < 0.8$, $0.8 < z < 1.5$) for each morphological type.

Key words. galaxies-evolution-adaptive optics-morphology

1. Introduction

The process of galaxy formation and the way galaxies evolve is still one of the most important unresolved problems in modern astrophysics. In the currently popular hierarchical picture of structure formation, galaxies are thought to be embedded in massive dark halos that grow from density fluctuations in the early universe (Fall & Efstathiou 1980) and initially contain baryons in a hot gaseous phase. This gas subsequently cools, and some fraction eventually condenses into stars. (Lilly et al. 1996; Madau et al. 1998). However, many of the physical details remain uncertain, in particular the process and history of mass assembly. One classical observational

* Based on ESO observations at VLT. Programmes P73.A-0814A and P75.A-0569A and 175.A-0839 (zCOSMOS).

** Based on observations obtained with MegaPrime/MegaCam, a joint project of CFHT and CEA/DAPNIA, at the Canada-France-Hawaii Telescope (CFHT) which is operated by the National Research Council (NRC) of Canada, the Institut National des Sciences de l'Univers of the Centre National de la Recherche Scientifique (CNRS) of France, and the University of Hawaii. This work is based in part on data products produced at TERAPIX and the Canadian Astronomy Data Centre as part of the Canada-France-Hawaii Telescope Legacy Survey, a collaborative project of NRC and CNRS.

way to test those models is classifying galaxies according to morphological criteria defined in the nearby Universe (Hubble 1936; de Vaucouleurs 1948; Sandage 1961) that can be related to physical properties and to follow this classification across time. (Abraham et al. 1996; Simard et al. 2002; Abraham et al. 2003). Indeed, since galaxies were recognized as distinct physical systems, one of the main goals in extragalactic astronomy has been to characterize their shapes. Comparison of distant populations with the ones found in the nearby Universe might help to clarify the role of merging as one of the main in galaxy evolution. (Cole et al. 2000; Baugh et al. 1996). Progress in this field has come from observing deeper and larger samples, but also from obtaining higher spatial resolution at a given flux and at a given redshift. In the visible, progress has been simultaneous on those two fronts, thanks in particular to the ultra-deep HDF fields observed with the Hubble Space Telescope. In particular, HST imaging has brought observational evidence that galaxy evolution is differentiated with respect to morphological type and that a large fraction of distant galaxies have peculiar morphologies that do not fit into the elliptical-spiral Hubble sequence. (Brinchmann et al. 1998; Wolf et al. 2003; Ilbert et al. 2006b). These results can however be biased by the fact that most of the sampled galaxies are at large redshift and are analyzed through their UV rest-frame emission which is more sensitive to star formation processes and to extinction. Moreover, it seems now clear that evolution strongly depends on the galaxy mass in the way that massive systems appear to have star formation histories that peak at higher redshifts whereas less massive systems have star formation histories that peak at progressively lower redshifts and are extended over a longer time interval (downsizing scenario). (Cowie et al. 1996; Brinchmann & Ellis 2000; Bundy et al. 2005). This could explain the fact that the population of massive E/S0 seems to be in place at $z \sim 1$ and evolve passively towards lower redshifts (De Lucia et al. 2006; Zucca et al. 2006). However, most of these studies are based on spectral type classifications and their interpretation in the framework of galaxy formation is not straightforward since galaxies move from a spectral class to another by passive evolution of the stellar populations.

In this context, high resolution near infrared observations are particularly important because the K-band flux is less dependent on the recent history of star formation, which peaks in the UV in rest frame, and gives thus a galaxy type from the distribution of old stars, more closely related to the underlying total mass than optical observations. This is why a large number of K-band surveys have been carried out using ground-based telescopes with different spatial coverages and limiting magnitudes in order to perform cosmological tests by means of galaxy counts essentially (Gardner et al. 1993; Glazebrook et al. 1995; McLeod et al. 1995; Bershady et al. 1998; McCracken et al. 2000; Maihara et al. 2001). However, no morphological information can be found due, in particular, to the seeing limited resolution, even with superb image quality as in the on-going CFHT/WIRCAM survey. Conselice et al. (2000) prove that only when the ratio of the angular diameter subtending $0.5h_{75}^{-1}kpc$ at a given distance to the angular

resolution of the image is around 1 reliable morphological estimators such as the asymmetry can be obtained.

Adaptive optics (AO) installed on ground based telescopes seems the only way today to obtain near-infrared high resolution data since no space observations are programmed until 2014 with JWST. The use of classical AO for deep surveys suffers, however, from inherent limitations such as the non-stationary PSF on long integration times and the finite isoplanetic field. This is why preliminary studies to probe the accuracy of adaptive optics are required, before launching very wide surveys. In particular, it is important to determine whether automated morphological classifications can be performed. Indeed, given the large number of galaxies, such automated methods for morphological classifications are desirable.

Minowa et al. (2005) published for the first time results based on adaptive optics observations. They achieved the impressive limiting magnitude of $K \sim 24.7$ with the Subaru Adaptive Optics system with a total integration time of $26.8hr$ over one single field of $1' \times 1'$. They proved that the use of adaptive optics significantly improves detection of faint sources but did not obtain morphological information. In a recently submitted paper, Cresci et al. (2006) performed a morphological analysis based on AO data for the first time. They observed a 15 arcmin^2 in the K_s band with NACO (SWAN survey) and classified distant galaxies into two morphological bins (Late Type, Early Type) by performing a model fitting with a Sersic law. They compared number counts and size-magnitude relation, for early and late-type separately, with hierarchical and Pure Luminosity Evolution (PLE) models respectively. They conclude that hierarchical models are not consistent with the observed number counts of elliptical galaxies and that PLE models are preferred. However, as discussed in several studies (Gardner 1998), despite that galaxy counts are still one of the classical cosmological tests, their interpretation remains difficult. It is not thus realistic to expect galaxy counts alone to strongly constrain the cosmological geometry or even to constrain galaxy evolution. A more complete study needs redshift estimates, which is lacking in the SWAN survey. That's the main reason why we have selected the COSMOS (Scoville & COSMOS Team (2005)) field to conduct our pilot programme since multi-wavelength photometric and spectroscopic observations are performed. This ensures a reliable redshift estimate for all our objects.

In this paper, we continue this AO validation task by morphologically classifying a sample of 79 galaxies observed using parametric (GIM2D, Simard et al. (2002)) and non-parametric (C-A, Abraham et al. (1994)) methods and comparing them. Fields, observed with NAOS/CONICA adaptive optics system are distributed over a 7 arcmin^2 area. We obtain for the first time an estimate of the distribution of galaxies in three morphological types (E/S0,S,Irr) at redshift $z \sim 1$ as measured from the near infrared at high spatial resolution. We then use the photometric redshifts to look for evolution clues as a function of morphology.

Field	α	δ	exp.time (s)	Seeing (arcsec)
STAR1	10:00:16	+02:16:22	10350	0.08
STAR2	10:00:52	+02:19:52	7650	-
STAR3	10:00:10	+02:06:08	7650	0.13
STAR4	09:59:52	+02:05:00	7170	0.14
STAR5	10:00:14	+02:09:09	10200	0.1
STAR6	10:00:02	+02:06:57	7650	0.15
STAR10	09:59:56	+02:04:07	10000	-

Table 1. Summary of observations for the seven analyzed fields. The mean seeing is estimated when faint stars were detected.

The paper proceeds as follows: the data set and the reduction procedures are presented in the next section. In § 3, we focus on the detection procedures and the sample completeness. In § 4 we discuss the estimate of redshifts using the multi-wavelength photometric data from COSMOS. The morphological analysis is discussed in section § 5 using Bulge/Disk decompositions and concentration and asymmetry estimators. Simulations for errors characterization are carried out for both classifications methods and comparisons between classifications are shown. In § 6 we compare the data with ground and space observations and use those comparisons to discuss morphological evolution in the last section. Throughout this paper magnitudes are given in the Vega system. We use the following cosmological parameters: $H_0 = 70 \text{ km s}^{-1} \text{ Mpc}^{-1}$ and $(\Omega_M, \Omega_\Lambda, \Omega_k) = (0.3, 0.7, 0.0)$.

2. The Data Set

7 fields of $1' \times 1'$ are observed in K_s band ($2.16 \mu\text{m}$) with the NAOS/CONICA assisted infrared camera installed on the VLT.¹ The fields are selected within the COSMOS survey area². In order to ensure a reliable AO correction, relatively bright stars ($V \sim 14$) were selected. We add a color criterium ($B - R < 1.0$) in order to benefit from a large attenuation of the flux in the near-IR and thus a smaller occultation of the central region of the images. The pixel scale ($0.054''$) is chosen to be twice the Shannon requirements with respect to the telescope diffraction limit in order to have larger fields. Although in the perfect correction case, the PSF FWHM would only be one pixel large, we will show in section 5 that adding some reduction procedures for the PSF reconstruction allows to overcome this difficulty, the more easily than in our data only a partial AO correction is reached. Indeed, this programme is pushed to its limits in terms of field size, exposure times and brightness of the guide star. On Fig. 1 are compared the mean radial profiles of 5 detected stellar objects.

Data are reduced in a standard way: exposures are taken in the auto-jitter mode, which means that the pointing is randomly shifted within a $7''$ box, in order to improve flat fielding, bad pixel correction and sky background withdrawal. Cosmic ray

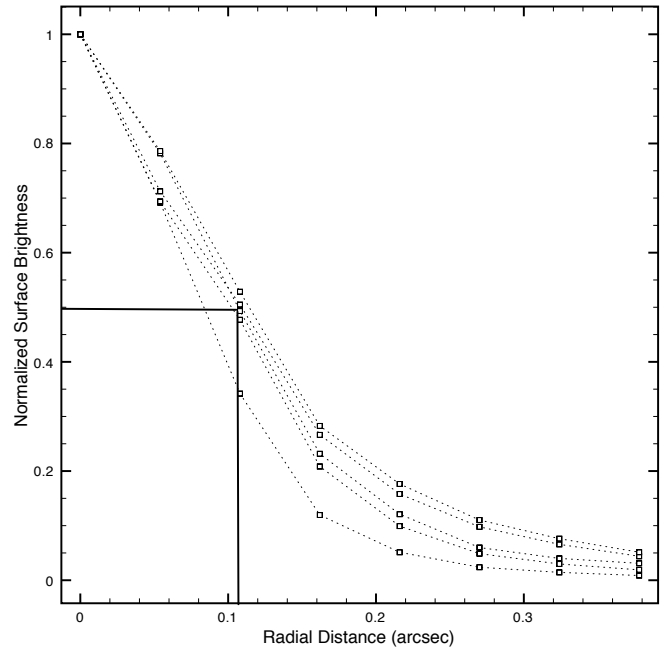


Fig. 1. Mean radial profile of all detected stellar objects with $K_s < 19$. The mean resolution is $\sim 0.1''$, broader than the telescope diffraction limit. This is a consequence of the long integration time ($\sim 3h$) and the large fields.

and flat corrections are applied, and recentering is done using a standard cross-correlation method.

Photometric zeropoints are determined using 2MASS stars (Kleinmann 1992). We perform aperture photometry on the guide stars and compare it to 2MASS data to deduce the zeropoints. Note that the change of detector between periods P73 and P75 resulted in different zeropoint values for each run. The average zeropoint for the first period is: 22.82 ± 0.06 and for the second period 23.29 ± 0.06 . We also use the ESO calibration data set standard stars (Persson et al. 1998) to validate our measurements (ESO pipeline computations and our own measurements on the standard stars images). There is good agreement between all these values.

3. Detection and Completeness

3.1. Detection

All objects having a 3σ signal above sky, over 4 four contiguous pixels are detected using SExtractor (Bertin & Arnouts 1996). We find 285 objects over the 7 fields. We then perform a cleaning task in order to separate galaxies from stars and spurious detections. This is made using the SExtractor MU_MAX and MAG_AUTO parameters that give the peak surface brightness above background and the Kron-like elliptical aperture magnitude respectively. Distribution of objects in this parameter space clearly defines three regions that separate extended sources from point-like or non-resolved sources and from spurious detections (Fig. 2). In this separation scheme, objects with very faint magnitude and high peak surface brightness are considered as glitches. Borders are drawn manually and a visual in-

¹ P73.A-0814A and P75.A-0569A

² <http://www.astro.caltech.edu/cosmos/>

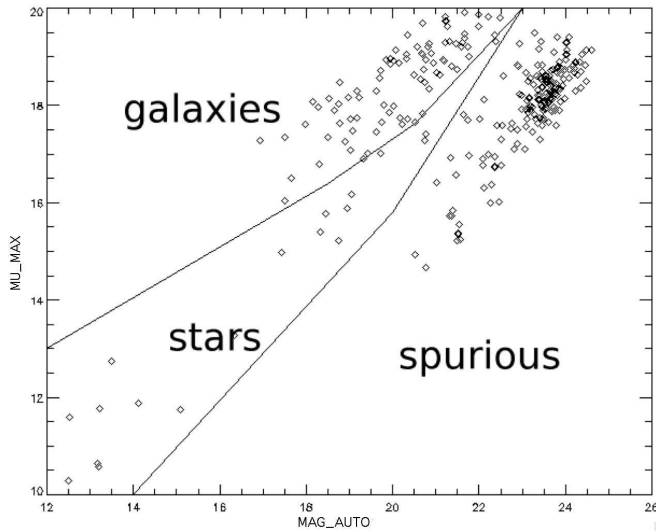


Fig. 2. Objects classification using the MAG_AUTO-MU_MAX plane; objects with high peak surface brightness and low global brightness are considered as glitches.

spection confirms that known stars in the field are indeed identified as point sources. We consequently identify 79 galaxies, 19 stars (or unresolved objects) and 187 spurious objects in the whole field.

3.2. Completeness

The sample completeness for point sources is estimated by creating artificial point sources from fields stars (see section 5 for detailed explanations) with apparent magnitudes ranging from $K_s = 18$ to $K_s = 24$ and placing them at random positions. We run SExtractor with the same configuration as for real sources and look for the fraction of detected objects. We find that the sample is 50% complete at $K_s = 22.5$ (or $AB = 24.5$) for point sources. Completeness for extended sources is estimated in a similar way: we generate 1000 galaxies with exponential and de Vaucouleurs profiles of different morphological types (bulge fraction ranging from 0 to 1) and with galactic parameters uniformly distributed. We find that the sample is 50% complete at $K_s = 21.5$ (or $AB = 23.5$) for extended sources (Fig. 4).

3.3. Galaxy Number Counts

The number densities of galaxies as a function of magnitude is a classical test of evolutionary and large-scale structure models (McCracken et al. 2000). Number counts can help to constrain the Universe models, and may provide constraints on the globally-averaged initial mass function. In order to make reliable measurements and compare them with previous ones, we apply several corrections to the raw numbers. Firstly we correct for completeness using the computed completeness for extended sources (see Fig. 4). Completeness changes as a function of the galaxy morphological type; we thus use the bulge fraction computed with GIM2D (see Section 5.2.2) to estimate the completeness for each detected galaxy. In that way, a galaxy

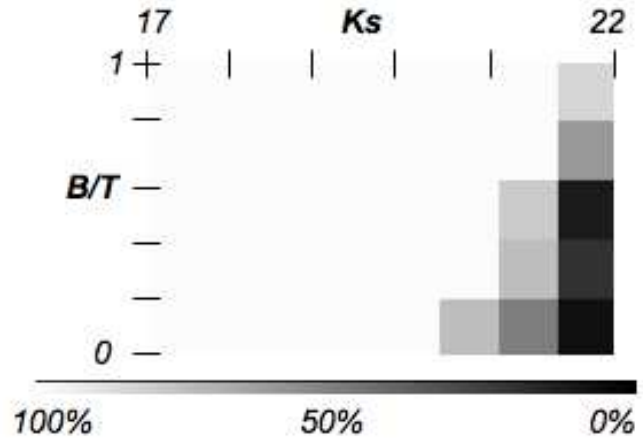


Fig. 4. Completeness for extended sources. Galaxies with galactic parameters ($r_d, r_e, B/T$) uniformly distributed are simulated and placed at random positions in the fields.

with a detection probability P_{det} , will be counted as $1/P_{det}$. In a second step, the number counts might also contain the counts from spurious detections due to the effect of statistical noise that becomes significant in the faint end. Those spurious detections are removed using the MAG_AUTO/MU_MAX plane as explained above (Fig. 2). Stellar objects are also removed at this step. Finally, errors in the determination of the objects photometry might result in a scatter of galaxy number counts among magnitude bins. In order to evaluate this effect we generated the probability matrix P_{ij} that gives the probability that an artificial object detected with magnitude m_i actually has a magnitude of m_j . We corrected the galaxy number counts accordingly. The results of our galaxy number counts are shown in Fig. 5.

We perform galaxy number counts up to $K_s = 22$. Above this magnitude limit, counts are no longer reliable as they must be corrected by a factor as large as the uncertainties; they are consequently not represented. We compute a power-law fitting in the range $17 < K_s < 22$ since the K-band number counts tend to show a slope change at $K \sim 17$ (Gardner et al. 1993). We find a mean slope of $d(\log N)/dm = 0.42 \pm 0.05$ which is in good agreement with previous works (McCracken et al. 2000; Bershady et al. 1998). This slope is however quite larger than the one derived from the SWAN observations (Cresci et al. 2006), also performed with an adaptive optics system. Indeed they claim to find a mean slope of $d(\log N)/dm = 0.26 \pm 0.01$ in the range $16 < K_s < 22$. As stated in Baker et al. (2003) the SWAN fields present however a selection bias at the bright end, since the fields were chosen to have an excess of bright galaxies: this could explain this difference despite that the excess becomes significant at $K_s < 16$ which is out of the computation range.

4. Photometric redshifts

Galaxy number counts are a useful description of galaxy populations but suffer from numerous degeneracies when trying to trace the evolution of galaxy populations. Model predictions

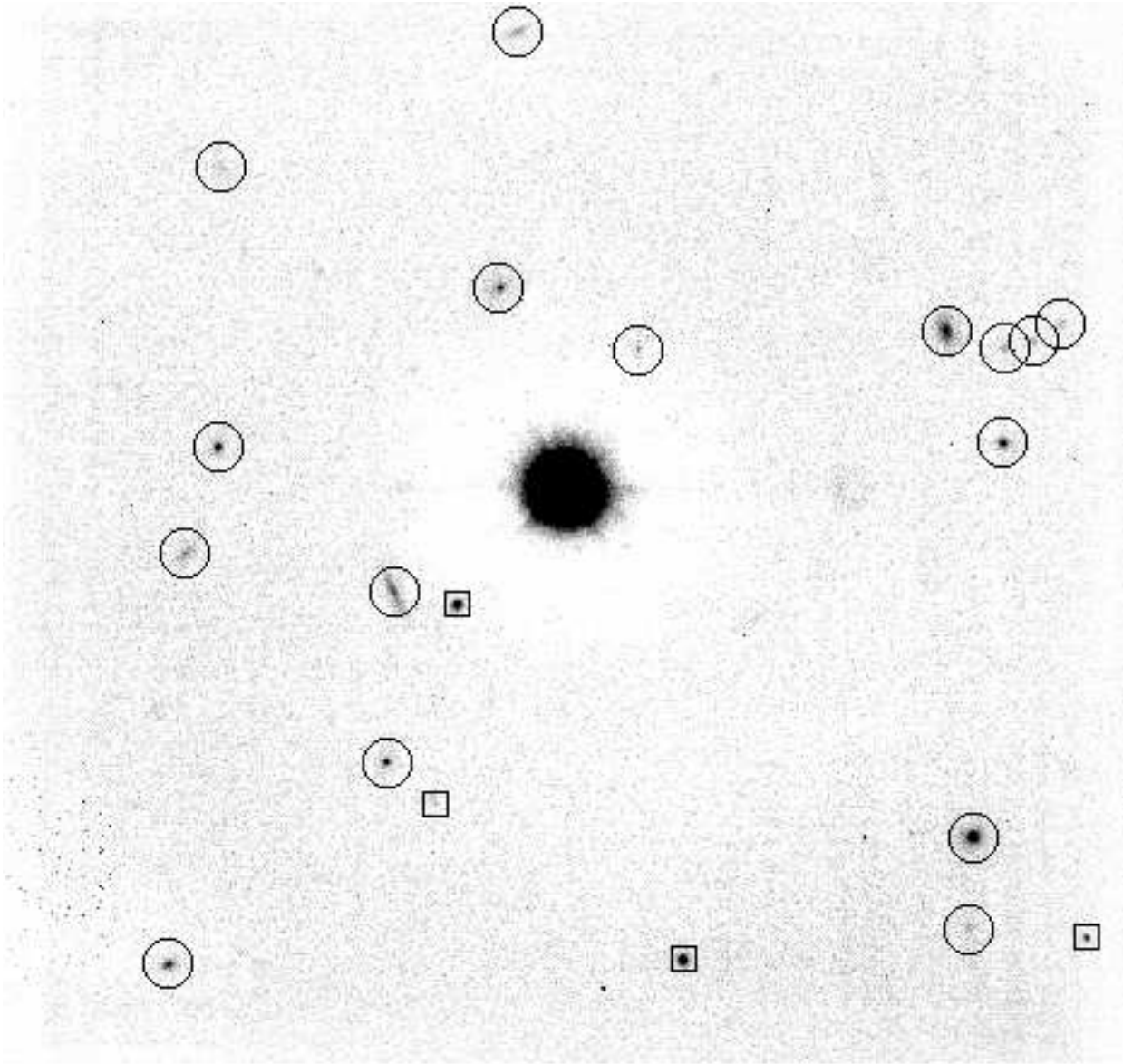


Fig. 3. NAOS/CONICA K_s -band image of the field centered at $\alpha = 10:00:16$, $\delta = +02:16:22$. The total integration time is 10350 s. The field size is $1' \times 1'$ with a pixel scale of 54 mas. Circles are detected galaxies and boxes are stars. The stellar FWHM is measured to be $0.1''$. The bright star at the center of the image is used as the AO guide star.

are subject to uncertainties in the spectral energy distributions and evolution of galaxies and in the free parameters specifying the luminosity function, the cosmological geometry, the number and distribution of galaxy types, and the effect of dust and merging. The need of having redshift information is therefore the reason for selecting the NACO fields within the ongoing Cosmic Evolution Survey (COSMOS) in which multi- λ and spectroscopic observations are performed. COSMOS is designed to probe the correlated evolution of galaxies, star formation, active galactic nuclei (AGN) and dark matter (DM) with large-scale structure (LSS) over the redshift range $z = 0.5$ to 3. The survey includes multi-wavelength imaging and spectroscopy from X-ray to radio wavelengths covering a 2 square deg area, including HST imaging of the entire field.

All these data are used for a direct estimate of the photometric redshifts of the galaxies detected in the NACO fields, computed with the code *Le Phare*³. A standard χ^2 method is implemented, including an iterative zero-point refinement combined with a template optimisation procedure and the application of a Bayesian approach (Ilbert et al. 2006a). We used 1095 spectroscopic redshifts taken from the zCOSMOS Survey (Lilly & The Zcosmos Team. 2006) to measure the photometric redshifts. This method allows to reach an accuracy $\sigma_{\Delta z}/(1+z_s) = 0.031$ with 1.0% of catastrophic errors, defined as $\Delta z/(1+z_s) > 0.15$.

The multi-color catalog of the COSMOS survey (Capack et al. 2006) consists of photometry measurements over a 3 arcsec-

³ http://www.lam.oamp.fr/arnouts/LE_PHARE.html

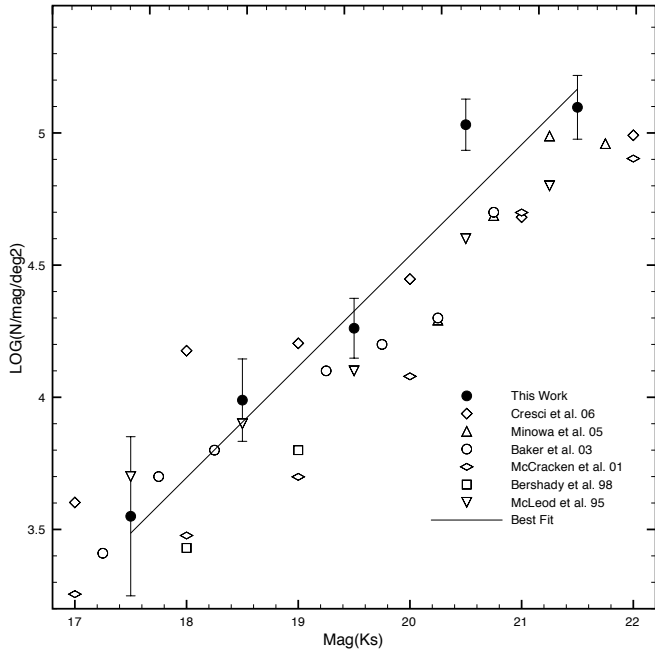


Fig. 5. K_s corrected number counts compared with other K -band surveys. The solid line is the best fitting power-law in the range $17 < K_s < 22$, with a slope $d \log(N)/dm = 0.42 \pm 0.05$. Error bars show poissonian errors.

ond diameter apertures for deep $B_j, V_j, g+, r+, i+, z+$ Subaru data taken with SuprimeCam, $u*, i*$ bands with MegaCam (CFHT), u', g', r', i', z' information from the Sloan Digital

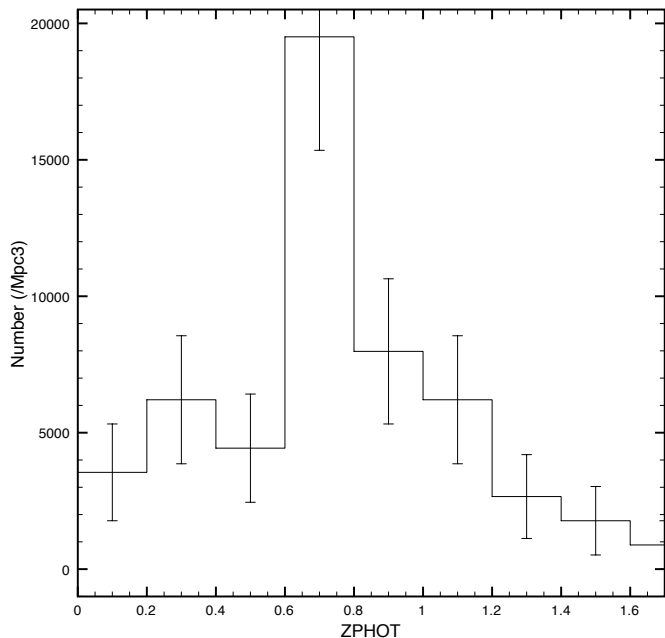


Fig. 6. Le Phare photometric redshift distribution for the 60 matched objects. The distribution is peaked around $z \sim 0.8$, in good agreement with the predictions of simple PLE models. Error bars show poissonian errors.

Sky Survey (SDSS), K_s magnitude from KPNO/CTIO, and $F816W$ HST/ACS magnitude. Objects are matched between the COSMOS and the NACO catalogues within a radius of $2''$ which takes into account possible astrometry differences between the catalogues. We match 60 objects out of the 79 detected in the NACO fields. Fig. 6 shows the photometric redshift distribution for these 60 matched objects. As expected for a galaxy sample limited to $K_s = 22$, the redshift distribution is peaked around $z \sim 0.8$ (Mignoli et al. 2005).

5. Automated Morphology Classifications

The 79 objects identified as extended sources are morphologically classified using two automated methods based on direct model fitting and on learning classification respectively. Automated classifications have the fundamental properties of being objective thus reproducible and they allow a precise error characterization. We proceed in two steps: first we detect irregular objects using asymmetry estimators and then we separate the regular objects between early and late type objects.

All along this section, we use extensive simulations for error estimates and calibration of the automated classifications as detailed further. For all the simulations, we assume that bulges are pure de Vaucouleurs profiles ($n = 4$) and that disks are exponential profiles. We then generate galaxies with parameters uniformly distributed in the following parameter space: $0 < B/T < 1$, $0'' < r_d < 0.7''$, $0'' < r_e < 0.7''$, $0^\circ < i < 70^\circ$ and $0 < e < 0.7$. Both bulge and disk position angles are fixed to 90° . The goal of these simulations is to characterize biases and errors; the uniformity of the parameter distributions adopted here is therefore perfectly suitable even though real galaxy parameters may not be so distributed. For the same reason, we do not take into account any redshift effect. Each simulation is convolved with the reconstructed PSF as explained in 5.2.2. The same PSF is used in both creating and analyzing the simulations, so the results will not include any error due to PSF mismatch. In order to simulate background noise, objects are embedded at random positions in the fields and detected with the same SExtractor parameters as for the real sources.

5.1. Irregular objects

The detection of objects presenting irregularities is made using the concentration and asymmetry estimators (Abraham et al. 1994; Abraham et al. 1996). Concentration is computed as the ratio of the flux between the inner and outer isophotes of normalized radii 0.3 and 1. Asymmetry (A) is obtained by rotating the galaxy image about its center by 180° and self-subtracting it to the unrotated image. The galaxy center is estimated by fitting a 2-D gaussian function to the galaxy. Since the absolute value for the residual light is used, noise in the images shows up as a small positive A signal even, in perfectly symmetrical objects. (Conselice et al. 2000). This is why we applied a noise correction to the computation: the value of A in a portion of

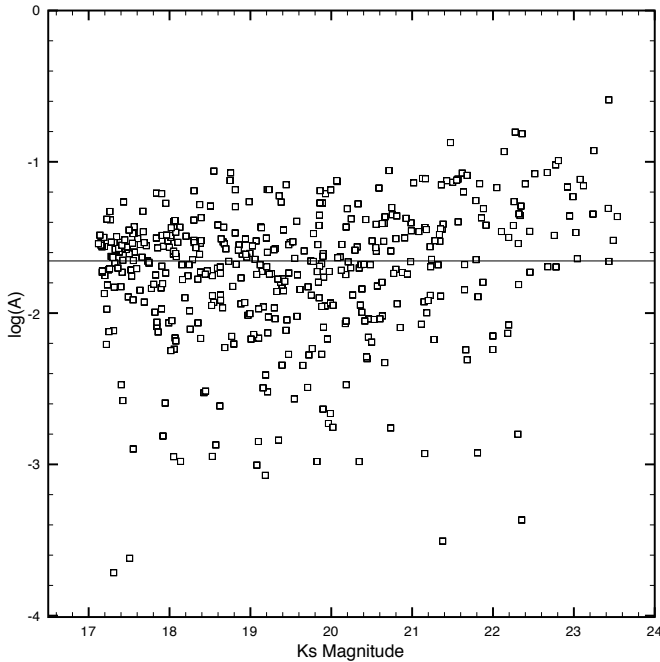


Fig. 8. Asymmetry versus magnitude: rotational asymmetry is affected by noise which can induce fainter objects to appear more asymmetric and introduce a bias in the number of irregular objects at the faint end of the sample. The figure shows that asymmetry begins to grow only at magnitudes greater than 22.2 which is greater than the limiting magnitude.

sky with area equal to that enclosed by the galaxy isophote. The definition of A that is used in the rest of the paper is:

$$A = \frac{1}{2} \left(\frac{\sum |I(i, j) - I_{180}(i, j)|}{\sum I(i, j)} - \frac{\sum |B(i, j) - B_{180}(i, j)|}{\sum I(i, j)} \right) \quad (1)$$

In order to establish the border between regular and irregular objects, a calibration of the C-A plane is needed. We thus simulate a set of galaxies with different galactic parameters and magnitudes ranging between $17 < K_s < 23$ that we embed in the real images. We compute the C and A parameters of these objects and plot the C-A plane. Since irregular objects cannot be simulated in a meaningful way, a kind of extrapolation is employed, based on two facts: a) irregular galaxies are supposed to have flatter photometric profiles (less concentrated) and to be more asymmetric than regular objects; b) those objects are not present in the simulated sample. We thus define the irregular zone as the upper left corner of the C-A plane where no simulated objects are found (Fig. 7).

As we previously said, rotational asymmetry is affected by noise even after correction. This means that fainter objects might appear more asymmetric and can thus induce a bias in the number of irregular objects at the faint end of the sample. To estimate this error, we plot the asymmetry parameter for a sample of 500 simulated galaxies with magnitudes ranging between $17 < K_s < 23$ (Fig. 8). The plot shows that asymmetry begins to be affected by noise only at magnitudes greater than 22.2, which is the magnitude limit of our working sample. In summary, we find the location of the irregular/peculiar objects

by simulating a set of regular galaxies and defining the peculiar area as the area outside. Then, we plot the observed data on this plane and count the galaxies in this peculiar area. We count 19 observed objects in this zone, i.e. 24% of the sample. We can attempt to quantify the error in this classification by considering the regular simulated objects that fall in the irregular zone. This gives the fraction of regular objects that are misclassified. We count 7 objects out of 500. Assuming that the error is symmetric, which means that the same fraction of irregular objects is classified as regular, we conclude that $24\% \pm 2.8$ of our sample corresponds to peculiar objects, in the magnitude range $17 < K_s < 22$

5.2. Regular objects: Late Type - Early Type Separation

5.2.1. CAS morphology

The positions of galaxies in the C-A plane are used to separate the early and late type galaxies as follows:

Calibration: A calibration of the C-A plane is needed before classification to investigate where the objects exactly fall. The strategy followed in this paper is two-fold: first we draw the irregular border as defined in Section 5.1. The border between early and late type objects can be deduced in a more automated way thanks to the analysis of simulated galaxies. We take the same 500 galaxies as above, for which the morphological type is known, and draw their positions in the C-A plane (Fig. 9). The border is then defined with a classification method based on Support Vector Machines (Vapnik 1995)⁴. Support Vector Machines (SVM) non-linearly map their n-dimensional input space into a "high dimensional feature space". In this high dimensional feature space, a linear classifier is constructed. SVM have two main parameters that can be changed: the kernel function and the tolerance C . The kernel function corresponds to the expected shape of the border: for instance if the objects are distributed with a gaussian distribution, then a gaussian kernel will be used. The adjustment of the border will also take into account a tolerance factor C : if C is high, the machine will not allow any object to be on the wrong side of the border. As a consequence, if the objects are strongly mixed in a given plane, the border can have a very complex shape. On the contrary, if C is too low the machine will not reach an optimal separation. In a first approach a linear kernel was used, assuming that the two family of objects can be separated with a linear function. Thus the C parameter is set to be infinite. The results of this separation are displayed in Fig. 9.

Accuracy: Automated classifications are useful because they allow a characterization of errors. To do so, once the borders are drawn, we generate another set of 500 fake objects with known morphology that we place again in the C-A plane and that we classify in the three morphological types we have defined. We then compare the results of our classification scheme with the

⁴ <http://www.isis.ecs.soton.ac.uk/resources/svminfo/>

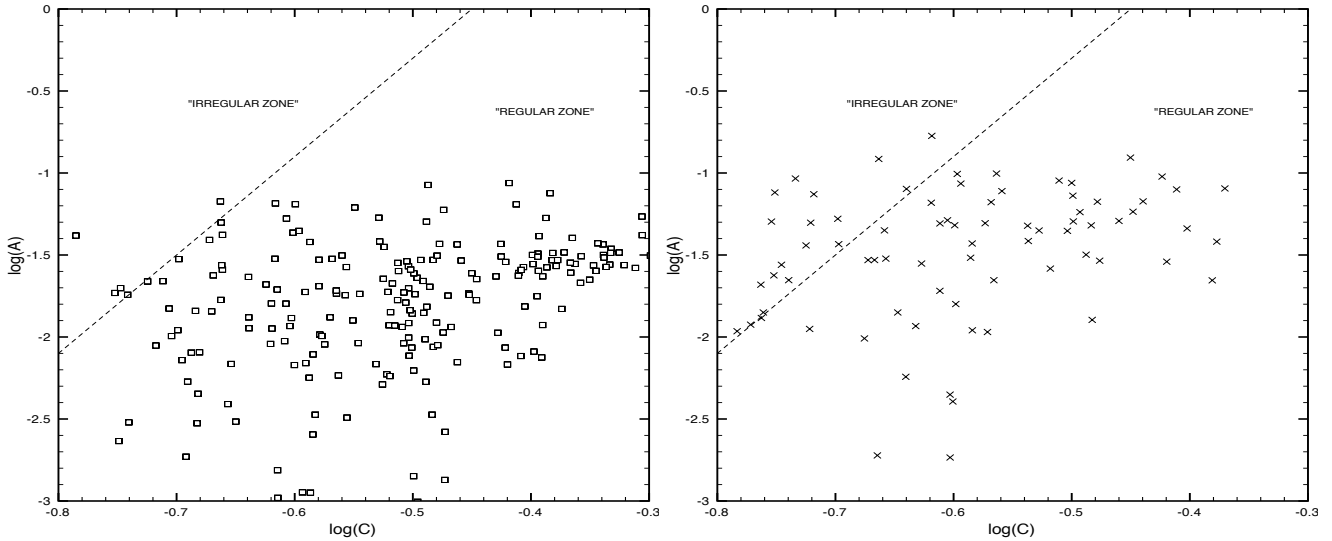


Fig. 7. Separation between regular and irregular objects. We simulate a set of galaxies and place them in the C-A plane. The border is built assuming that no simulated galaxies must fall in the irregular zone and that irregular objects are expected to be less concentrated and more asymmetric than regulars. Left: simulated objects (Empty Squares), Right: real objects (Crosses) .

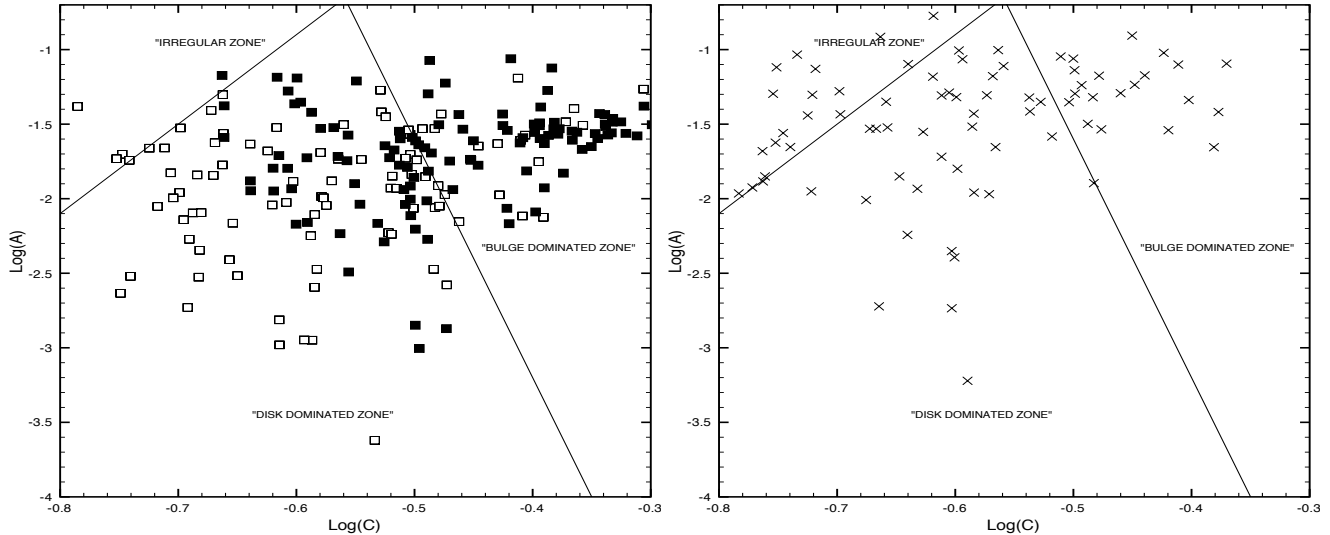


Fig. 9. CAS calibration and classification. We simulate galaxies with different bulge fractions as if they were observed by NACO and place them in the C-A plane. Borders are drawn using an automated classification method (SVM) which avoids the use of a nearby sample and subjective visual classifications. Left: simulated objects, open squares: objects with $B/T < 0.2$, filled squares: objects with $B/T > 0.8$. Right: real objects. .

initial morphological type. Errors are estimated in magnitude bins, from $K_s = 18$ to $K_s = 22$ (Table 2). We achieve 70% of good identifications up to $K_s = 21$ ($AB = 23$) and 66% up to our magnitude limit $K_s = 22$. That means that we are able to classify galaxies in the three main morphological types with reliable accuracy at least up to $K_{AB} = 23$.

Some words about the C-A plane: At first sight, the distribution of galaxies in our C-A plane looks significantly different that what has been reported in previous works using this technique. (Abraham et al. 1996; Brinchmann et al. 1998) . Indeed, the slope of the separating border between bulge and

disk dominated galaxies has been found to be positive whereas the one found here is negative, although previous classification are somewhat arbitrary. As a consequence elliptical galaxies lie on the top right corner of the plane in our classification rather than in the bottom right corner in most other studies. There might be several reasons to explain this effect:

- As NACO images are undersampled, highly concentrated objects lie only over a few pixels and, consequently, even a small mismatch in the determination of the rotation center can lead to important asymmetries. To check this effect we computed concentration and asymmetry parameters for

Magnitude	Correct Identifications
$K_s < 19$	80%
$K_s < 20$	73%
$K_s < 21$	70%
$K_s < 22$	66%

Table 2. Error estimates of the CAS classification. We simulate a set of galaxies with known morphologies, classify them into the three morphological classes using the computed borders in the C-A plane and look for mismatches. The accuracy decreases with increasing magnitudes.

the detected point like sources. We find that, indeed, they appear to have higher asymmetric values than the galaxies.

- It might also be a consequence of the method used for the borders estimate. Abraham et al. (1996) and Brinchmann et al. (1998) used a visual inspection based on a local survey and, in order to account for the effects of redshift, they applied corrections to the concentration parameter. In this work, we used a fully automated method based on simulations which reproduce very closely the observational conditions and on learning classification methods. So no correction is in principle needed, but this gives a different border. The question that consequently arises is whether the differences in the borders produce important differences in the classification procedure. All this points are fully discussed in Section 6 thanks to detailed comparisons with space observations of the sample.

5.2.2. Model Fitting Morphology

The second method is based on a direct two components fitting with exponential and de Vaucouleurs profiles, using GIM2D (Simard et al. 2002). The 2D galaxy model used by GIM2D has 11 parameters that are fitted to the real data. The most important ones are the total flux and the bulge fraction B/T ($= 0$ for pure disk systems). Other parameters are the disk scale radius r_d and the disk inclination i , the effective radius r_e and the ellipticity e of the bulge component, and other geometric parameters for the center and orientation of both components.

PSF reconstruction: In order to obtain reliable results, GIM2D needs a noise-free, well-sampled PSF. This is why special attention has been paid to PSF reconstruction. Here, classical methods such as DAOPHOT or Tiny Tim could not be used for two reasons. First, the Adaptive Optics PSF has a specific shape which is neither ‘seeing limited like’ nor ‘spatial like’. An AO system operated with a guide star of moderate brightness ($V \sim 14$) can only partially correct for turbulence-induced distortions. This partially corrected PSF consists of two components: a diffraction-limited core, superimposed on a seeing halo. Second, in order to have a larger field and a better sensitivity, data were under-sampled by a factor 2 (0.054'' pixel scale whereas 0.02'' is needed to be Nyquist sampled).

We developed a simple algorithm that uses field stars to generate Shannon sampled PSFs by means of a fitting procedure

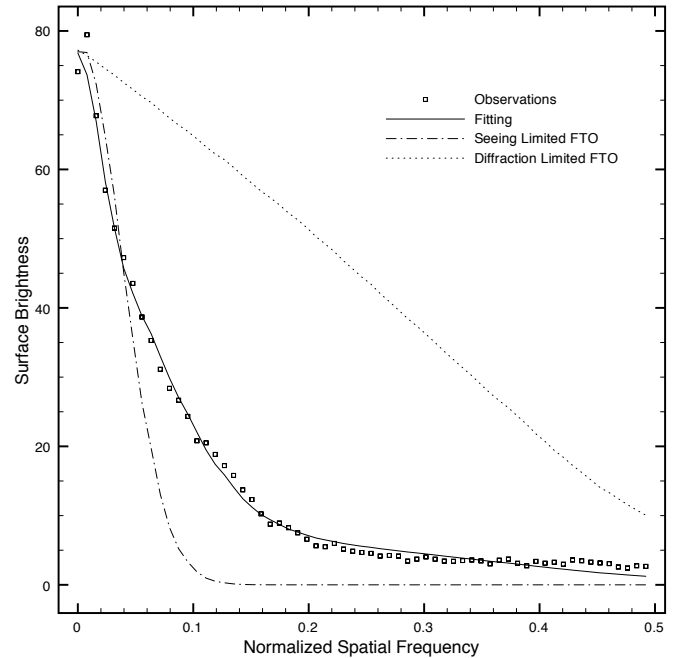


Fig. 10. Example of PSF fitting in the Fourier space. Squares: observations, dashed line: seeing limited MTF, dotted line: diffraction limited MTF. The AO MTF contains higher frequencies than the seeing limited one. The telescope diffraction limit is however not reached in this example due to the undersampling of the instrumental setup.

in the Fourier Space. The process is as follows: we generate an artificial PSF, with a diffraction-limited core and a gaussian halo, with the following distribution

$$\text{PSF}_{art}(x, y) = k \left[\text{SR} \times A(x, y) + (1 - \text{SR}) \times \exp\left(-\frac{x^2 + y^2}{\sigma^2}\right) \right]$$

where SR is the Strehl ratio, $A(x, y)$ is the bi-dimensional Airy function, σ is the gaussian dispersion which can be related to the seeing and k is a normalisation factor. This artificial PSF is built with a Shannon sampling, binned by a factor 2 to reach the real image pixel scale and finally Fourier transformed to create a simulated MTF (Power Spectrum). On the other hand, for each observed star, its Fourier transform is fitted with the simulated MTF. The parameters estimated that way (SR, σ and k) are then used to build an estimate of the PSF with the correct Shannon sampling.

Working in the Fourier Space avoids including the background estimate and PSF position as a fit parameter, which is particularly delicate in our case, since the FWHM is less than 2 pixels large. In the few cases where the fitting procedure does not converge a second gaussian halo is added. Fig. 10 shows the result of the fitting for one star in the spatial frequency domain. In this paper, we do not consider variations in the PSF caused by adaptive optics such as anisoplanatism but we are working in building a complete model for PSF estimate for future observations.

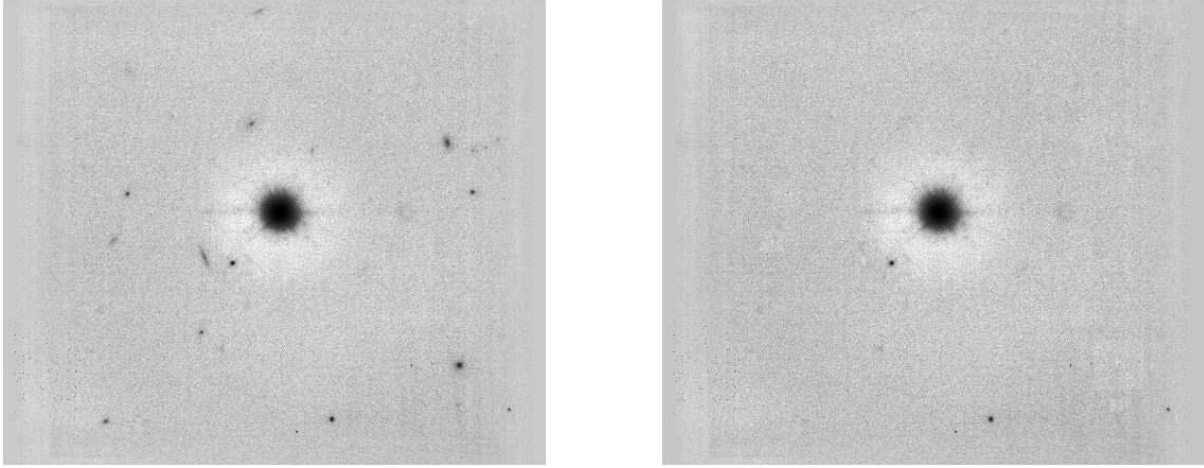


Fig. 11. Original (left panel) and residual (right panel). We have subtracted the GIM2D models to the original image and look for residual objects. Left: original image, Right: image after model subtraction. Only the objects identified as point sources remain.

Error analysis: We run GIM2D on the 79 objects with magnitudes ranging between $K_s = 17 - 22$, using a two components model and the artificial PSF built as described above. The fitting converged for the whole sample, and the results are quite convincing in terms of residual images. Fig. 11 shows the result of subtracting the models to the original image. It can be seen that only the three objects identified as stars in Fig. 3 remain in the residual image. We therefore consider that reliable morphological information can be obtained up to the magnitude limit $K_s = 22$.

Visual inspection of the models compared to the real images (Fig. 12) also reveals a good agreement, in particular for bright sources. For the faintest objects, however, it is more difficult to estimate the fitting accuracy. This is why objective and systematic error characterization is needed. To do so we generate a sample of 1000 synthetic galaxies with known galactic parameters uniformly distributed: $0 < B/T < 1$, $0 < r_d < 0.5''$, $0 < r_e < 0.5''$, $0 < e < 0.7$, $0^\circ < i < 85^\circ$. The Sersic bulge index was fixed at $n = 4$ and both bulge and disk position angles were fixed to 90° . As explained in Simard et al. (2002), the goal of these simulations is to characterize biases and errors; the uniformity of the parameter distributions adopted here is therefore perfectly suitable even though real galaxy parameters may not be so distributed. Each simulation is convolved with the reconstructed PSF. The same PSF is used in both creating and analyzing the simulations, so the results will not include any error due to PSF mismatch. In order to simulate background noise, objects are embedded at random positions in the fields and detected with the same SExtractor parameters as for the real sources. Finally, the GIM2D output files are processed through the same scripts to produce a catalog of final recovered structural parameters.

Following the Simard et al. (2002) procedure, we decide to represent errors in a set of two-dimensional maps giving systematic and random errors at each position. The GIM2D parameter space is a complex space with 11 dimensions so these maps can only offer a limited representation of the complex multidimensional error functions but makes interpretation much simpler. The error analysis presented in this paper will

focus on the error made on the main morphological estimator, the bulge fraction, as a function of two main parameters: apparent magnitude and half light radius. Table 3 precisely shows in details the sources of errors on B/T as a function of galaxy magnitude and half-light radius.

Error maps show that uncertainty on bulge fraction for objects fainter than $K_s = 19$ (AB=21) is lower than 20%. This is comparable to what is obtained for the brightest objects in the I-band with HST (Simard et al. 2002). For fainter magnitudes, systematic errors rise significantly which means that we underestimate bulge fractions. This is a well known GIM2D effect for low S/N ratio objects (Simard et al. 2002): the outer wings of steep surface brightness profiles such as the $r^{1/4}$ profile are hidden in low signal-to-noise objects and this artificially decreases the recovered bulge fraction. But for most of the objects brighter than $K_s = 19$ galactic parameters can be estimated correctly ($\sigma < 0.2$ and $b < 0.1$), even for small objects ($r_{hl} < 0.3''$) of size comparable the limits of space observations (see Section 6).

5.3. Results of the analysis and comparison of classifications

We classified the galaxies into three main morphological types according to the fitting results. One of the main results is that about $25\% \pm 2.8\%$ of our sample corresponds to peculiar or irregular objects (19 objects out of 79). For the rest of the sample, the GIM2D analysis finds 22 ($\sim 22\%$) of bulge dominated galaxies ($B/T > 0.5$) and 38 ($\sim 53\%$) of disk dominated ($B/T < 0.5$) while for the CAS classification, we find 42 ($\sim 48\%$) of spiral galaxies and 18 ($\sim 27\%$) of elliptical ones.

Looking in more details into the reliability of the two classification schemes, we do a one-to-one comparison of the morphological types assigned by the GIM2D analysis or the CAS one (Fig 13): we compute the probability that a galaxy classified using the GIM2D classification is classified with the same morphological type by CAS. The probability is computed by dividing the number of galaxies in each morphological CAS bin by the total number of galaxies of the same type selected

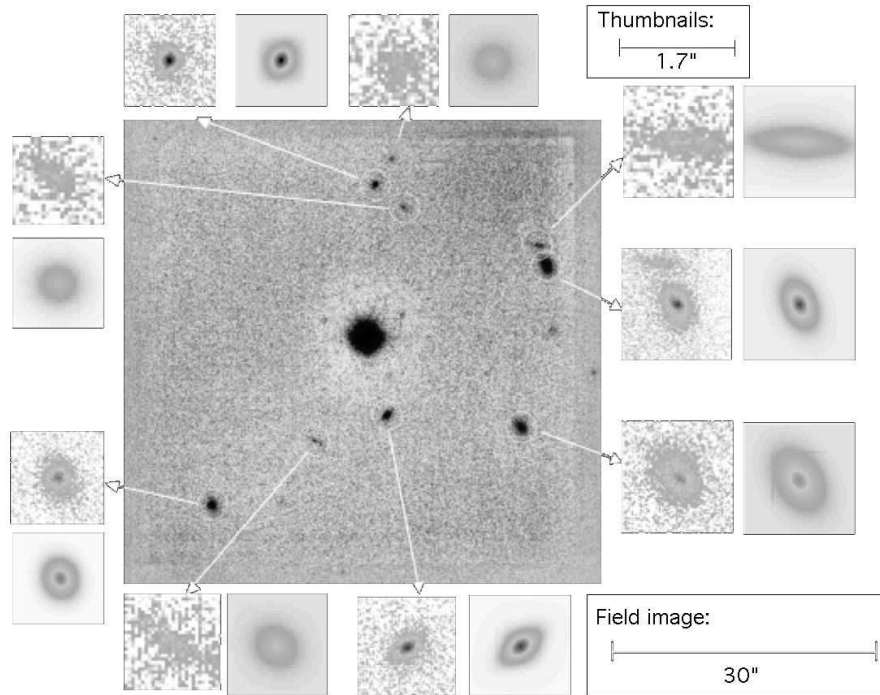


Fig. 12. GIM2D models for one field. The small thumbnails show the real and the model galaxy. For bright galaxies there is a good agreement. For the faintest ones it is difficult to estimate the accuracy of the model. This is why systematic error estimations are necessary.

Magnitude	$-1 < \log(r_{hl}) < -0.75$			$-0.75 < \log(r_{hl}) < -0.5$			$-0.5 < \log(r_{hl}) < -0.25$			$-0.25 < \log(r_{hl}) < 0$		
	b	σ	N	b	σ	N	b	σ	N	b	σ	N
[17 – 17.5]	N/A	N/A	(0)	-0.13	0.3	(11)	-0.04	0.15	(26)	-0.03	0.06	(8)
[17.5 – 18]	0.16	0.13	(2)	0.05	0.17	(8)	0.05	0.24	(26)	0.01	0.11	(11)
[18 – 18.5]	N/A	N/A	(0)	0.02	0.21	(24)	0.14	0.18	(50)	0.12	0.12	(14)
[18.5 – 19]	0.16	0.19	(2)	-0.01	0.38	(18)	0.11	0.26	(59)	0.10	0.08	(9)
[19 – 19.5]	0.13	0.23	(2)	-0.09	0.27	(44)	0.12	0.30	(39)	0.14	0.10	(6)
[19.5 – 20]	0.05	0.20	(7)	0.19	0.26	(47)	0.06	0.19	(21)	N/A	N/A	(0)
[20 – 20.5]	0.34	0.33	(10)	0.23	0.30	(52)	0.01	0.38	(10)	N/A	N/A	(0)
[20.5 – 21]	0.38	0.31	(9)	-0.08	0.37	(30)	N/A	N/A	(0)	N/A	N/A	(0)

Table 3. Error analysis on the bulge fraction B/T for different magnitude ranges and different bins in galaxy size. The galaxy size is represented by the half-light radius and is distributed in 4 bins in $\log(r_{hl})$. In the top left corner bright and small objects are found whereas faint and large objects are placed in the bottom right corner. b is the average difference between initial and recovered values of B/T while σ is the dispersion. N is the number of simulations used for each bin.

with GIM2D. Overall, there is a good agreement between both classifications in the whole sample: the probability that a spiral galaxy identified by GIM2D has the same morphological type in CAS classification is $p = 0.75$ and $p = 0.65$ for bulge dominated galaxies including the faintest objects ($K_s < 23$). For irregulars it is obviously $p = 1$ since the detection procedure is the same in both methods.

There might be two reasons why the classifications are not exactly the same: First, the S/N ratio might cause discrepancies. Indeed, as we show in Section 5.2.2, at low S/N ratio GIM2D tends to under-estimate the bulge fraction. This implies that some galaxies detected by GIM2D as disk dominated are in fact detected as bulge dominated by CAS. Fig. 13 shows the

effect of reducing the limiting magnitude to $K_s = 20$: the fraction of objects classified as bulge dominated by GIM2D and CAS rises up to 0.85. Second, it might be a problem of definition. Indeed, the morphological bins are not exactly the same in both classifications. In particular, objects with intermediate morphological type (i.e. $B/T \sim 0.5$) might cause discrepancies. If we remove those objects from the sample all the bulge dominated objects and 90% of the disk dominated objects detected by GIM2D are also detected by CAS with the same classification.

Anyway, the comparison of both classifications allows a quantification of the error in classification of regular galaxies in the sense that it seems reasonable to think that the true value

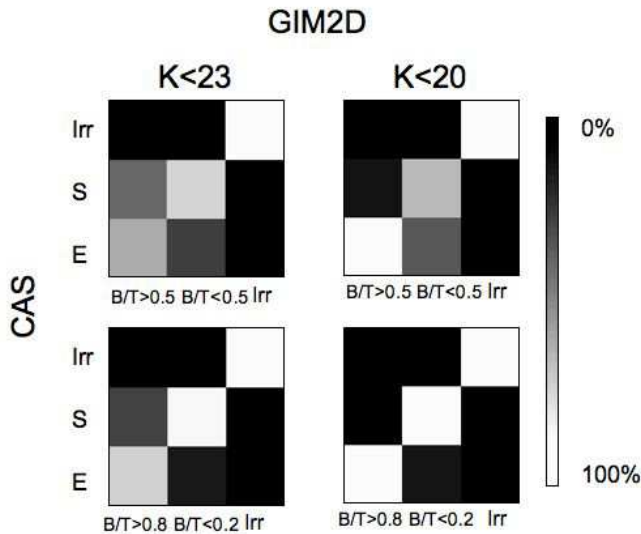


Fig. 13. Comparison of classification methods. The figure shows the probability that a galaxy classified with GIM2D is classified in the same morphological type by CAS. (see text for details).

should be somewhere between the two results. GIM2D estimate gives thus a lower-limit for the early-type fraction and CAS the upper-limit and vice versa for the late-type fraction. This way, we conclude that the mixing of population in our sample is: $24.5\% \pm 2.5\%$ of early-type galaxies, $49.5\% \pm 1.5\%$ of late-type galaxies and $24\% \pm 2.8\%$ of irregular/peculiar galaxies.

Our results offer for the first time a direct measurement of the distribution of galaxy in three morphological types at $z \approx 1$ from high spatial resolution imaging in the K-band. We observe that the fraction of 25% of irregular objects at $z = 1$ is significantly higher than the fraction of these objects in the local Universe, confirming from rest-frame data at ~ 1 microns the well documented trend of this population increasing with redshift (e.g. Brinchmann et al. (1998)). However this result must be taken with caution. Indeed GIM2D accuracy falls for objects fainter than $K_s = 19$, which represents 80% of the sample. Moreover at the faint end, the fraction of irregular objects can be over estimated because of the low signal-to-noise ratio. But there are good reasons to consider this result significant: even though there is an over estimation of disks in the faint end, the morphological classification bins are large enough to reduce the number of false classifications. Indeed, even in the zones where the random error in the bulge fraction estimate is ~ 0.3 or larger we will not classify a pure bulge ($B/T \sim 1$) as a disk.

6. Comparison with ground-based and HST observations

In this section we compare our AO observations with ground based and space observations.

6.1. Ground based observations

Effective radii of local galaxies, except for compact dwarf galaxies, range from ~ 1.0 to ~ 10 kpc depending on their luminosity (Bender et al. 1992; Impey et al. 1996). Our spatial resolution of $\sim 0.1''$ corresponds to about 1 kpc at $z \sim 1$; we are in principle able to determine morphological types even at $z > 1$. Thus, in order to estimate the performance of AO deep imaging and to justify the automated morphology classification, we compared our images with deep I-band seeing-limited images taken from the Canada-France-Hawaii Telescope Legacy Survey (CFHTLS)⁵. One of the so-called Deep fields is centered on the COSMOS field, although it is smaller than the total COSMOS area (1 square degree out of 2). Here we used the release T0003 images (March 2006)⁶, especially the deep i' one, corresponding to a total integration time of 20 hours, with an average FWHM of $\sim 0.7''$.

We compare real data by selecting a galaxy classified as a disk by GIM2D and CAS in the NACO data and comparing it to the results obtained with CFHTLS data. The surface brightness profile is fitted with both with a PSF-convolved de Vaucouleurs profile and an exponential profile. Figure 15 shows that with seeing limited observations, it is more difficult to establish a clear separation between both profiles, even if the determination of the brightness profile is possible at much larger distance thanks to the depth of the images and the low noise level of the sky background. So although ultra-deep sub-arcsecond imaging is powerful in terms of high number statistics, thanks to the wide field coverage, we consider that it is more rewarding to look at a smaller sample of galaxies, but with more reliable morphology determinations thanks to the spatial gain of the AO.

6.2. Space Observations

We compare our images with space data taken from the COSMOS survey. Since our observed fields were selected within the COSMOS area, the same objects are observed with the HST-ACS in the I-band at high spatial resolution. We thus morphologically classify the 60 objects for which the photometric redshift are known (sec. 4). We use those results to both estimate the effect of the observation band on morphology and to validate our method to divide the C/A plane. The C-A estimators were calibrated with simulations using the same method as for the K band data. Fig. 19 shows the C-A plane cut. We again find a negative slope for the border between disk and bulge dominated objects. We find for the whole sample $31\% \pm 1.6\%$ irregulars, $43\% \pm 1.5\%$ spirals and $23\% \pm 2.5\%$ ellipticals.

6.2.1. Rest Frame Morphologies

Even if the global morphological distribution is quite similar in the I and K bands, there are some differences when we look at each object individually (Fig. 16). In particular, there are un-

⁵ <http://www.cfht.hawaii.edu/Science/CFHTLS/>

⁶ <http://terapix.iap.fr>

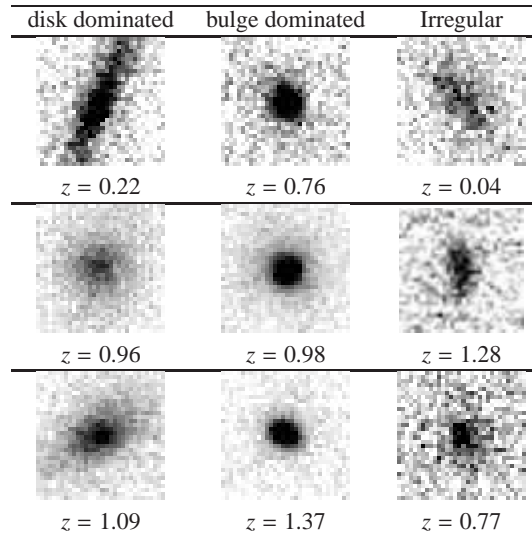


Fig. 14. Example of classification in the three main morphological types at different redshifts. The images size is $1.7' \times 1.7'$

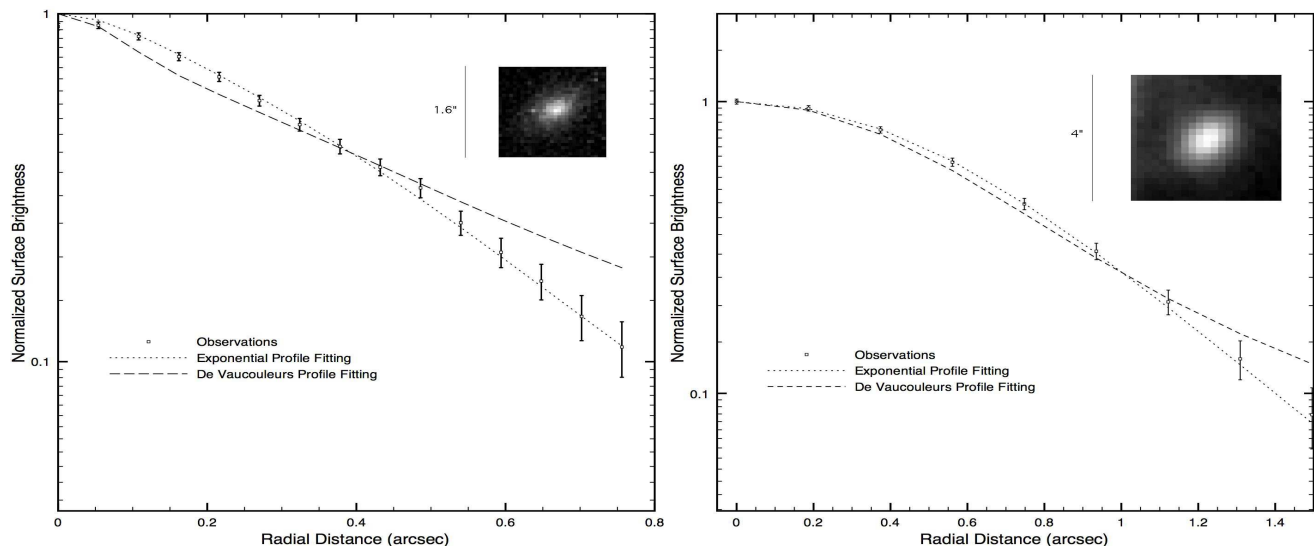


Fig. 15. Comparison with ground based observations. We perform a profile fitting on the same real galaxy observed with NACO (left) and MegaCam (CFHTLS- i' band, right). The galaxy magnitude is $K_{AB} = 20.5$ and $i' = 21.3$. The fit is done with a pure de Vaucouleurs and exponential profile. While in the MegaCam data it is difficult to establish which one is the better solution in the NACO image we can clearly see that an exponential profile gives better results.

certainties between K irregulars and I spirals and between I spirals and K ellipticals.

These differences might come from the fact that we are not observing in the same photometric bands and consequently not probing the same stellar populations. In order to correctly compare both classifications we need to correct the measurements to estimate how galaxies would look like if they were observed locally.

As a matter of fact, Brinchmann et al. (1998) showed that high- z galaxies imaged by HST differ in appearance from their local counterparts because of their reduced apparent size and sampling characteristics, a lower signal-to-noise ratio and reduced surface brightness with respect to the sky background and a shift in the rest wavelength of the observations. These

effects combine to give some uncertainty in the morphological classifications of galaxies.

The first effect is a change in the concentration value measured at low redshift. Indeed, Brinchmann et al. (1998) draw the borders in the C-A plane using a local sample (Frei et al. 1996) visually classified. However, the concentration value depends on redshift, since the threshold is defined relative to the sky. Thus, less of the galaxy is sampled because of cosmological dimming. The solution they adopted is to correct C for this effect. We do not need a correction of the concentration in this paper because we use simulations that reproduce exactly the observing conditions to calibrate the C-A plane. The result, is that borders are moved with respect to a local classification instead of changing the C value.

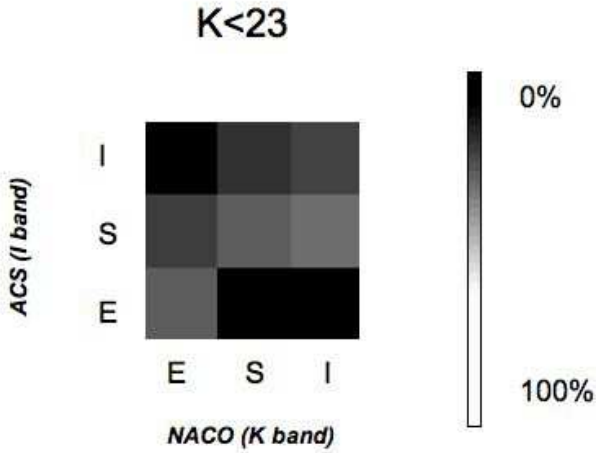


Fig. 16. Galaxy Distribution: comparison between K-band and I band C-A classifications. The figure shows the probability that a galaxy in the K-band is classified in the same morphological type in the I-band.

The shift in the rest frame wavelength of observations is however more difficult to estimate. Indeed the question that arises here is to determine whether the morphological type estimated at high redshift would be the same if observed at low redshift. When observing a galaxy in the K-band at redshift $z \sim 1$ the equivalent rest frame wavelength will be around the z band, however when observed in the I-band the rest frame will be around the B band. That implies that it can exist a mismatch in the morphological classification since we are not probing the same morphological blocks. To correct from this effects we need to 'move the objects' into a common rest frame wavelength. This is the called morphological k correction. The method employed by Brinchmann et al. (1998) consists in determining the morphology from a local sample, redshift the objects using SED models and look at the fraction of galaxies that move in to an other morphological class. A drift coefficient that characterizes the drift from category X to category Y is thus defined:

$$D_{XY} = \frac{N_{X \rightarrow Y}}{N_X} \quad (2)$$

Once the fraction of missclassified objects is determined, the observed number of objects in class X can be related to the true number:

$$N_X^{obs} = N_X + \sum N_Y D_{YX} - N_X \sum D_{XY} \quad (3)$$

Here we proceed as follows: Brinchmann et al. (1998) computed the coefficients to shift from the I observed morphology to the R rest frame morphology. So, we use those coefficients to correct the observed HST morphology of our sample to the one observed in the R rest frame band, since the filter used for observations is the same (F814W). Once we have this corrected morphology we can compare it to the NACO uncorrected morphology. This can be done because the observed sample is exactly the same in the K and in the I-band. So, if

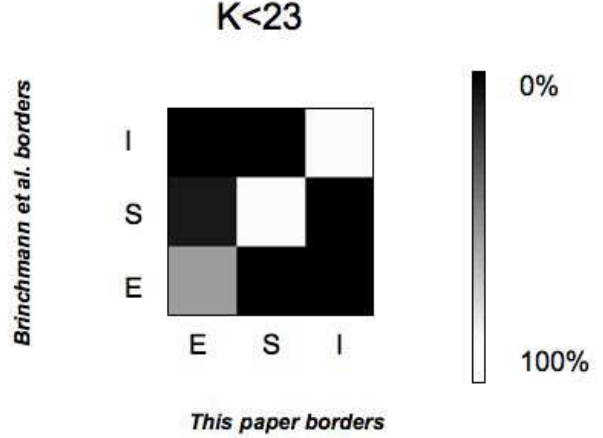


Fig. 17. Comparison of classifications with different borders. We repeat the morphological classification with the borders used by Brinchmann et al. (1998). We conclude that the results do not change significantly which supports the validity of the employed method.

we were in the same rest-frame band, we should find the same morphology.

We use the coefficients computed by Brinchmann et al. (1998) to correct the ACS morphology and divide the sample into two redshift bins ($z < 0.8$ and $z > 0.8$). Results are shown in figure 18.

- At low redshift ($z < 0.8$) the corrected I-band distributions and the non corrected K-band are similar.
- At higher redshift, the K-band distribution tends to give a larger fraction of bulge dominated objects than the I-band data. The irregular objects are consistent with the corrected distributions. So the excess seems to come from the disk dominated objects, as if there was a fraction of disk dominated objects that move to the bulge dominated zone. Those issues are fully discussed in 7.

6.2.2. About borders

As we said in previous sections the computed borders of the C-A plane are different from what can be found in the literature. Previous works have been done in the I-band using HST imaging (Abraham et al. 1996; Brinchmann et al. 1998). As we have a sample observed in the I-band we are able to establish whether the change in the borders has significant consequences in the morphological classifications. To do so, we classified the I-band sample using the Brinchmann et al. (1998) borders and compared the results to the ones obtained with our method (Fig. 17). We find that there are no significant discrepancies between both classifications. We conclude that our method is valid and has moreover the key advantage to be free of subjective judgments.

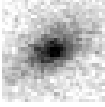
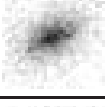
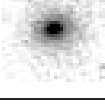
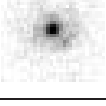
NACO			ACS	
morph. type	image	Zphot	image	morph. type
Disk dom.		1.090		Irr.
Irr.		0.4223		Irr.
Disk dom.		0.6689		Irr.
Bulge dom.		1.17460		Disk dom.

Table 4. *Morphological k correction:* morphological differences when observing in the K and I-bands. The same objects observed in the K and I bands present different morphologies. The images size is $1.7' \times 1.7'$

7. Discussion: Evolution considerations

Figure 18 shows the redshift distribution of the sample for the three main morphological types. The effective number of objects per bin is small (~ 30), so it's difficult to establish strong conclusions. However, it seems clear that the fraction of irregulars is higher compared to local surveys. Indeed this doesn't seem to be an artifact due to the low signal-to-noise ratio since it's consistent with the ACS morphology in the I-band. For early and late objects, conclusions are less clear from our still small sample. In the low redshift bin, there is no significant difference between the rest-frame R band and the non corrected K-band population, which indicates that when observing in the K-band there is no need of *morphological k correction*. However, we find an excess of bulge dominated objects in the high redshift bin, which cannot be seen in the I corrected band (Fig. 18). This can be caused by the fact that the drift coefficients computed by Brinchmann et al. (1998) might contain errors. Since they are based on SED fitting, it's logical to think that errors are more important for high redshift objects. This would explain why the results are consistent at low redshift. It can also be a consequence of the size of the sample: as the number of objects per bin is small, errors in the classification of a small fraction can lead to discrepancies between the two bands. This issue will certainly be solved with a larger sample.

8. Summary and Conclusions

We analyzed the morphologies of a sample of 79 galaxies in the near-infrared thanks to adaptive optics imaging at a resolution of $0.1''$. Thanks to extensive simulations, we showed that adaptive optics can be used to obtain reliable high resolution morphological information in an automated way, and is thus adapted to large observation programmes:

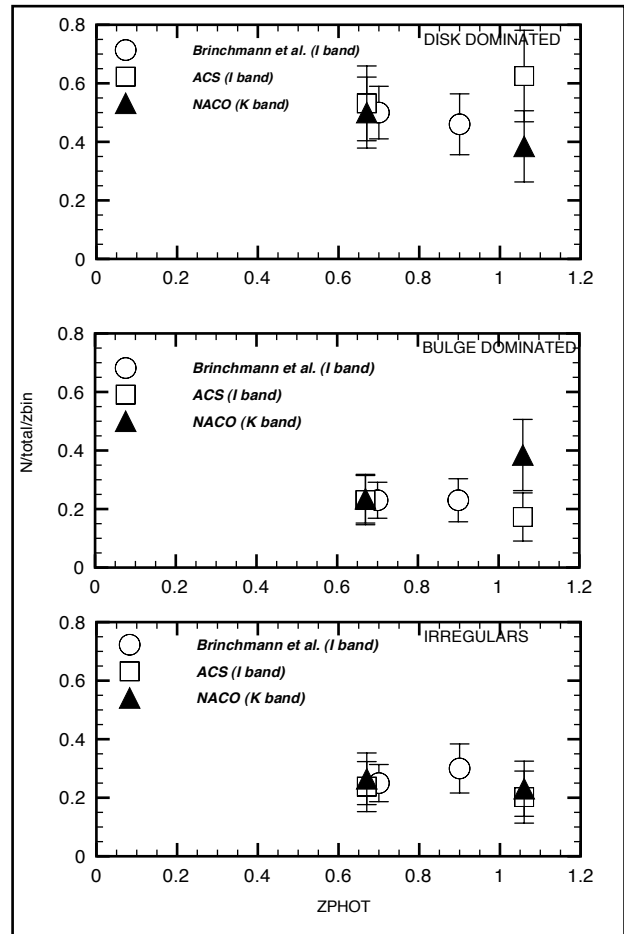


Fig. 18. Redshift Distribution for the three morphological types. We plotted the Brinchmann et al. (1998) sample (circles) and our sample observed with ACS (squares) and with NACO (triangles). Brinchmann et al. (1998) and ACS data are corrected to the R rest-frame band. The NACO sample is observed from the K-band and no correction has been applied. The ACS and NACO samples have been separated into two redshift bins ($z < 0.8$ and $z > 0.8$). The represented redshifts are the median redshifts of each bin.

- Galactic parameters (bulge fraction, disk scale length, bulge effective radius) can be estimated by means of model fitting with errors lower than 20% up to $K_s = 19$. This is comparable with space data.
- Galaxies can be separated into three main morphological bins up to $K_s = 21$, with at least 70% of good identifications and 66% up to $K_s = 22$.
- For fainter galaxies ($22 < K_s < 23$) the accuracy of the morphological classification decreases. Simulations show that bulge dominated and disk dominated galaxies can be separated with only 55% accuracy at $K_s = 23$.

We obtain, for the first time an estimate of the mix of morphological types of the galaxy population up to $z \approx 1$ from ground based K-band observations with high spatial resolution comparable or better to visible imaging from space. We demon-

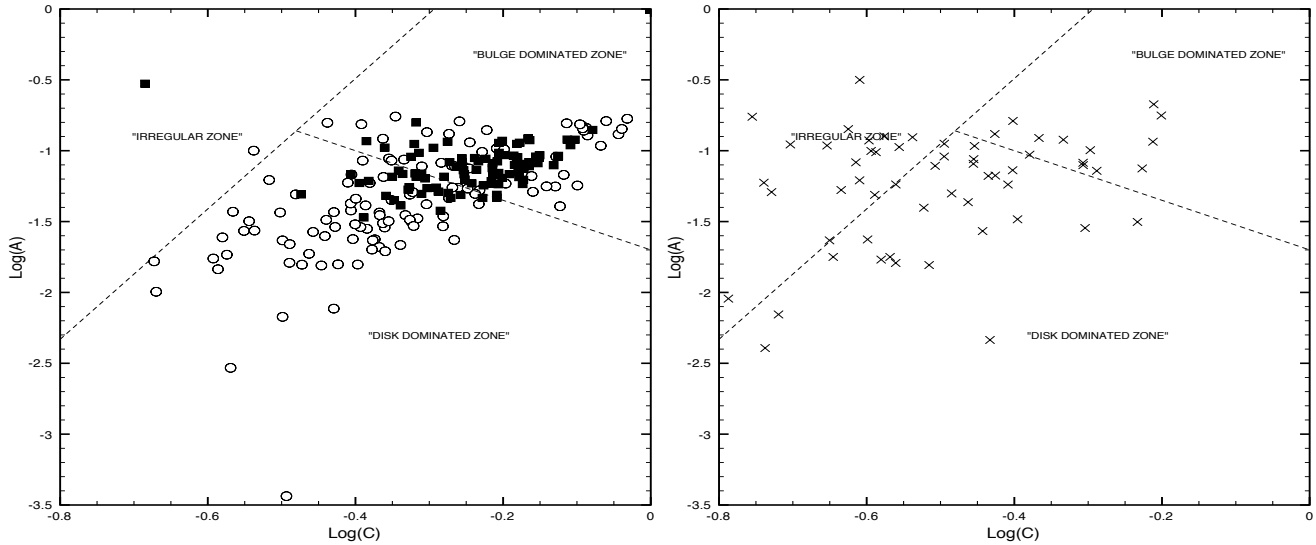


Fig. 19. CAS cut for the ACS images. The same classification procedure has been repeated for the same sample observed with ACS in the I-band. Left: simulated objects. Right: real objects. Circles: $B/T < 0.2$, Filled squares: $B/T > 0.8$, Crosses: real objects

strate that estimating morphology from K-band data at $z \approx 1$ is not affected by *morphological k correction*, as there is no significant difference between our population and the corrected I-band population. Despite the still small sample at hands, the galaxy counts are demonstrated to be in good agreement with previous works. We find that the fraction of irregulars at $z \approx 1$ is about $24\% \pm 2.8\%$ using automated classification methods. This is higher than what is found in local surveys, confirming the well established trend of an increasing fraction of irregular galaxies with redshift as observed from surveys in the visible. Our small sample does not allow to reach firm conclusions on the evolution of the fraction of late-type or early-type galaxies, but classifying galaxies from K-band AO imaging data is demonstrated to be reliable.

From this work it seems clear that adaptive optics can be used for observational cosmology with reliable accuracy and data of this type should contribute to a better understanding of galaxy evolution in the coming future. However it still remains a new technique and technical difficulties exist such as variable PSF, small fields, subsampling, need of guide stars that make the use of classical reduction methods more difficult. This is now easier with laser guide stars becoming available and new sets of utilities such as we are developing to enable easy data processing and analysis of adaptive optics data for the community. This opens the way to observing large samples required to reach a robust statistical accuracy. We are planning to enlarge our sample by observing a large number of areas around bright stars in the COSMOS field, which will strongly reduce uncertainties in the study of morphological evolution.

References

- Abraham, R., van den Bergh, S., Glazebrook, K., et al. 1996, ApJ Supplement, 107, 1
- Abraham, R. G., Valdes, F., Yee, H. K. C., & van den Bergh, S. 1994, ApJ, 432, 75
- Abraham, R. G., van den Bergh, S., & Nair, P. 2003, ApJ, 588, 218
- Baker, A. J., Davies, R. I., Lehnert, M. D., et al. 2003, A&A, 406, 593
- Baugh, C. M., Cole, S., & Frenk, C. S. 1996, MNRAS, 283, 1361
- Bender, R., Burstein, D., & Faber, S. M. 1992, ApJ, 399, 462
- Bershady, M. A., Lowenthal, J. D., & Koo, D. C. 1998, ApJ, 505, 50
- Bertin, E. & Arnouts, S. 1996, A&AS, 117, 393
- Brinchmann, J., Abraham, R., Schade, D., et al. 1998, ApJ, 499, 112
- Brinchmann, J. & Ellis, R. S. 2000, ApJ, 536, L77
- Bundy, K., Ellis, R. S., & Conselice, C. J. 2005, ApJ, 625, 621
- Cole, S., Lacey, C. G., Baugh, C. M., & Frenk, C. S. 2000, MNRAS, 319, 168
- Conselice, C. J., Bershady, M. A., & Jangren, A. 2000, ApJ, 529, 886
- Cowie, L. L., Songaila, A., Hu, E. M., & Cohen, J. G. 1996, AJ, 112, 839
- Cresci, G., Davies, R., Baker, F., et al. 2006, astro-ph/0607221
- De Lucia, G., Springel, V., White, S. D. M., Croton, D., & Kauffmann, G. 2006, MNRAS, 366, 499
- de Vaucouleurs, G. 1948, Annales d'Astrophysique, 11, 247
- Fall, S. M. & Efstathiou, G. 1980, MNRAS, 193, 189
- Frei, Z., Guhathakurta, P., Gunn, J. E., & Tyson, J. A. 1996, AJ, 111, 174
- Gardner, J. P. 1998, PASP, 110, 291
- Gardner, J. P., Cowie, L. L., & Wainscoat, R. J. 1993, ApJ, 415, L9
- Glazebrook, K., Peacock, J. A., Miller, L., & Collins, C. A. 1995, MNRAS, 275, 169
- Hubble, E. 1936, ApJ, 415
- Ilbert, O., Arnouts, S., McCracken, H. J., et al. 2006a, ArXiv Astrophysics e-prints

- Ilbert, O., Lauger, S., Tresse, L., et al. 2006b, *A&A*, 453, 809
- Impey, C. D., Sprayberry, D., Irwin, M. J., & Bothun, G. D. 1996, *ApJS*, 105, 209
- Kleinmann, S. G. 1992, in *ASP Conf. Ser. 34: Robotic Telescopes in the 1990s*, ed. A. V. Filippenko, 203–212
- Lilly, S. & The Zcosmos Team. 2006, *ApJ*, in press
- Lilly, S. J., Le Fevre, O., Hammer, F., & Crampton, D. 1996, *ApJ*, 460, L1+
- Madau, P., Pozzetti, L., & Dickinson, M. 1998, *ApJ*, 498, 106
- Maihara, T., Iwamuro, F., Tanabe, H., et al. 2001, *PASJ*, 53, 25
- McCracken, H. J., Metcalfe, N., Shanks, T., et al. 2000, *MNRAS*, 311, 707
- McLeod, B. A., Bernstein, G. M., Rieke, M. J., Tollestrup, E. V., & Fazio, G. G. 1995, *ApJS*, 96, 117
- Mignoli, M., Cimatti, A., Zamorani, G., et al. 2005, *A&A*, 437, 883
- Minowa, Y., Kobayashi, N., Yoshii, Y., et al. 2005, *ApJ*, 629, 29
- Nakamura, O., Masataka, F., Brinkmann, J., & Schneider, D. P. 2003, *AJ*, 125, 1682
- Persson, S. E., Murphy, D. C., Krzeminski, W., Roth, M., & Rieke, M. J. 1998, *AJ*, 116, 2475
- Sandage, A. 1961, *The Hubble atlas of galaxies* (Washington: Carnegie Institution, 1961)
- Scoville, N. Z. & COSMOS Team. 2005, in *Bulletin of the American Astronomical Society*, 1309–+
- Simard, L., Willmer, C. N. A., Vogt, N. P., et al. 2002, *ApJS*, 142, 1
- Tasca, L. & White, S. 2005, *astro-ph/0507249*
- Vapnik, V. 1995, Springer-Verlag, 536
- Wolf, C., Meisenheimer, K., Rix, H.-W., et al. 2003, *A&A*, 401, 73
- Zucca, E., Ilbert, O., Bardelli, S., et al. 2006, *A&A*, 455, 879

Table .1. Summary of the morphological classifications for the 79 detected objects. For each object we show the I and K band magnitudes and the estimated morphological type from AO imaging in the K-band (with GIM2D and CAS) and from HST-ACS in the I-band.

Object ID	RA	DEC	Ks mag.	I mag.	ZPHOT	GIM2D(K-band)	CAS(K-band)	CAS(I-band)
1	150.069	2.26541	20.18	99.50	99.9000	Disk Dom.	Disk Dom.	N/A
2	150.068	2.27872	20.70	22.42	0.711700	Disk Dom.	Disk Dom.	Irr
3	150.072	2.27703	22.87	24.14	0.247200	Disk Dom.	Disk Dom.	Disk Dom.
5	150.068	2.27552	19.76	24.22	1.78470	Disk Dom.	Disk Dom.	Irr
6	150.063	2.27500	18.70	99.50	99.9000	Disk Dom.	Disk Dom.	N/A
7	150.061	2.27509	22.16	23.39	0.832200	Bulge Dom.	Disk Dom.	Bulge Dom.
9	150.062	2.27487	22.01	23.75	0.793700	Disk Dom.	Disk Dom.	Bulge Dom.
10	150.062	2.27478	21.32	99.50	99.9000	Disk Dom.	Disk Dom.	N/A
11	150.067	2.27476	21.75	22.64	0.0400000	Bulge Dom.	Bulge Dom.	Disk Dom.
13	150.072	2.27355	20.09	23.44	0.956100	Bulge Dom.	Bulge Dom.	Disk Dom.
14	150.072	2.27223	20.23	99.50	99.9000	Irr	Irr	N/A
15	150.062	2.27360	19.81	99.50	99.9000	Bulge Dom.	Bulge Dom.	N/A
16	150.070	2.27174	19.02	20.92	0.219100	Disk Dom.	Disk Dom.	Irr
19	150.070	2.26963	20.38	22.79	0.740000	Bulge Dom.	Bulge Dom.	Bulge Dom.
22	150.062	2.26870	18.57	21.83	0.875600	Bulge Dom.	Bulge Dom.	Disk Dom.
27	150.062	2.26755	22.24	22.74	0.475700	Bulge Dom.	Bulge Dom.	Bulge Dom.
30	150.072	2.26712	20.01	23.81	1.33790	Disk Dom.	Disk Dom.	Disk Dom.
32	150.222	2.32621	18.53	21.35	0.886100	Disk Dom.	Disk Dom.	Irr
33	150.216	2.33658	22.68	22.64	0.810100	Bulge Dom.	Disk Dom.	Disk Dom.
34	150.217	2.33579	19.21	21.94	0.832600	Disk Dom.	Bulge Dom.	Disk Dom.
36	150.216	2.33511	21.91	23.63	0.818800	Irr	Irr	Irr
37	150.212	2.33398	20.20	21.84	0.514000	Irr	Irr	Disk Dom.
38	150.212	2.33337	17.68	19.97	0.400600	Disk Dom.	Disk Dom.	Irr
40	150.217	2.32890	18.74	20.86	0.670000	Disk Dom.	Bulge Dom.	Irr
41	150.213	2.32853	18.35	20.81	0.739400	Disk Dom.	Disk Dom.	Irr
42	150.219	2.32814	20.88	22.78	0.799500	Irr	Irr	Disk Dom.
45	150.047	2.10808	17.72	19.91	0.506000	Bulge Dom.	Bulge Dom.	Bulge Dom.
47	150.042	2.10673	19.58	22.76	0.987200	Disk Dom.	Bulge Dom.	Bulge Dom.
52	150.048	2.10486	19.52	21.06	0.270200	Disk Dom.	Disk Dom.	Disk Dom.
54	150.043	2.10360	20.31	99.50	99.9000	Disk Dom.	Disk Dom.	N/A
56	150.045	2.10348	20.55	99.50	99.9000	Irr	Irr	N/A
59	150.041	2.10279	21.29	99.50	99.9000	Disk Dom.	Disk Dom.	N/A
76	149.964	2.08732	20.86	21.18	0.671400	Irr	Irr	Disk Dom.
79	149.975	2.08549	21.87	23.29	0.703700	Disk Dom.	Disk Dom.	Disk Dom.
81	149.968	2.08319	19.96	99.50	99.9000	Disk Dom.	Disk Dom.	N/A
84	149.968	2.08286	21.76	99.50	99.9000	Bulge Dom.	Bulge Dom.	N/A
95	149.968	2.08006	21.37	99.50	99.9000	Irr	Irr	N/A
99	149.971	2.07970	20.27	23.92	0.754600	Disk Dom.	Bulge Dom.	Irr
103	149.965	2.07890	21.10	23.67	1.37440	Disk Dom.	Bulge Dom.	Bulge Dom.
105	150.058	2.14397	22.42	22.78	0.240300	Disk Dom.	Bulge Dom.	Bulge Dom.
108	150.064	2.15644	19.52	21.14	0.979400	Bulge Dom.	Bulge Dom.	Bulge Dom.
111	150.058	2.15569	21.09	99.50	99.9000	Bulge Dom.	Disk Dom.	N/A
113	150.058	2.15551	21.20	23.58	0.994000	Bulge Dom.	Disk Dom.	Disk Dom.
114	150.059	2.15517	19.58	23.51	1.26360	Bulge Dom.	Bulge Dom.	Disk Dom.
117	150.063	2.15427	23.05	99.50	99.9000	Bulge Dom.	Disk Dom.	N/A
119	150.068	2.15348	21.67	23.04	0.935900	Disk Dom.	Disk Dom.	Disk Dom.
123	150.058	2.15258	21.41	22.79	1.08450	Irr	Irr	Disk Dom.
133	150.058	2.15105	21.43	23.59	1.11800	Irr	Irr	Disk Dom.
145	150.064	2.14850	20.90	23.92	1.16300	Irr	Irr	Irr
148	150.067	2.14840	22.17	99.50	99.9000	Bulge Dom.	Disk Dom.	N/A
170	150.015	2.11984	20.52	22.36	0.714900	Irr	Irr	Irr
175	150.015	2.11842	19.05	22.48	1.17460	Disk Dom.	Bulge Dom.	Disk Dom.
177	150.007	2.11780	17.00	18.82	0.338100	Disk Dom.	Disk Dom.	Disk Dom.

Table .1. continued.

Object ID	RA	DEC	Ks mag.	I mag.	ZPHOT	GIM2D(K-band)	CAS(K-band)	CAS(I-band)
182	150.011	2.11709	20.43	99.50	99.9000	Disk Dom.	Disk Dom.	N/A
183	150.004	2.11697	21.76	22.43	0.787500	Irr	Irr	Disk Dom.
184	150.013	2.11682	18.84	22.26	1.06140	Disk Dom.	Disk Dom.	Irr
185	150.011	2.11655	17.62	99.50	99.9000	Disk Dom.	Bulge Dom.	N/A
190	150.004	2.11461	19.43	20.61	0.698200	Bulge Dom.	Disk Dom.	Bulge Dom.
195	150.009	2.11392	18.83	21.37	0.689900	Disk Dom.	Disk Dom.	Disk Dom.
200	150.013	2.11341	20.35	21.95	0.422300	Irr	Irr	Irr
203	150.013	2.11180	21.37	23.45	0.770500	Irr	Irr	Disk Dom.
205	150.009	2.11151	20.89	21.58	0.334700	Disk Dom.	Disk Dom.	Disk Dom.
214	150.009	2.10981	21.49	99.50	99.9000	Irr	Irr	N/A
220	149.987	2.07308	19.84	23.65	1.00700	Disk Dom.	Disk Dom.	Irr
223	149.987	2.07260	22.64	22.73	1.10000	Disk Dom.	Disk Dom.	Irr
224	149.982	2.07236	20.85	22.43	0.689900	Disk Dom.	Disk Dom.	Bulge Dom.
227	149.982	2.07204	21.32	22.77	0.624900	Disk Dom.	Disk Dom.	Bulge Dom.
234	149.985	2.07137	20.84	22.33	0.0400000	Irr	Irr	Bulge Dom.
243	149.985	2.07027	19.33	99.50	99.9000	Disk Dom.	Bulge Dom.	N/A
245	149.983	2.07019	22.90	23.40	0.525700	Irr	Irr	Bulge Dom.
251	149.987	2.06838	20.34	23.95	1.54810	Bulge Dom.	Bulge Dom.	Disk Dom.
252	149.983	2.06874	18.95	22.07	1.20850	Disk Dom.	Bulge Dom.	Bulge Dom.
254	149.982	2.06801	20.40	23.84	1.48830	Irr	Irr	Irr
259	149.984	2.06707	21.22	99.50	99.9000	Disk Dom.	Disk Dom.	N/A
268	149.983	2.06630	21.23	23.82	0.881200	Irr	Irr	Irr
270	149.986	2.06550	18.00	21.40	0.794100	Disk Dom.	Bulge Dom.	Irr
274	149.984	2.06479	19.30	21.73	0.668900	Disk Dom.	Disk Dom.	Irr
277	149.985	2.06474	22.14	23.89	0.743900	Disk Dom.	Disk Dom.	Disk Dom.
285	149.989	2.06312	21.82	23.80	0.214600	Disk Dom.	Disk Dom.	Disk Dom.